Gate-Tunable Spin XOR Operation in a Silicon-Based Device at Room Temperature

Ryoma Ishihara,[1] Yuichiro Ando,[1,*] Soobeom Lee,[1] Ryo Ohshima[1], Minori Goto,[2] Shinji Miwa,[2] Yoshishige Suzuki,[2] Hayato Koike,[3] and Masashi Shiraishi[1,†]

[1]*Department of Electronic Science and Engineering, Kyoto University, Kyoto, Kyoto, Japan*
[2]*Graduate School of Engineering Science, Osaka University, Toyonaka, Osaka, Japan*
[3]*Advanced Products Development Center, TDK Corporation, Ichikawa, Chiba, Japan*

Room-temperature operation of a spin exclusive-OR (XOR) gate is demonstrated in lateral spin-valve devices with nondegenerate silicon (Si) channels. The spin XOR gate is a fundamental part of the magnetologic gate that enables reconfigurable and nonvolatile NAND or OR operation in one device. The device for the spin XOR gate consists of three iron (Fe)/cobalt (Co)/magnesium oxide (MgO) electrodes (i.e., two input electrodes and one output electrode). Spins whose spin angular momentum corresponds to the binary input 1 or 0 are injected into the Si channel from the input electrodes. The spin-drift effect is controlled by a lateral electric field in the Si channel to adjust the spin-accumulation voltages under two different parallel configurations, corresponding to (1, 1) and (0, 0), so that they exhibit the same value. As a result, the spin-accumulation voltage detected by the output electrode exhibits three different voltages, represented by an XOR gate. The one-dimensional spin-drift–spin-diffusion model clearly explains the XOR behavior obtained. Charge-current detection of the spin XOR gate is also demonstrated. The detected charge current has a maximum of 1.67 nA, the highest value in spin XOR gates reported thus far. Furthermore, gate-voltage modulation of the spin XOR gate is also demonstrated, which enables operation of multiple magnetologic gate devices.

I. INTRODUCTION

Logic gates using electron spins are expected to realize beyond-complementary-metal-oxide-semiconductor (CMOS) architectures, which exhibit superior switching energy and high logic density compared with the traditional CMOS architecture. Furthermore, they also provide the ability to integrate logic with nonvolatile storage in ferromagnetic memory. Whereas a variety of proposals for logic operation based on spin-dependent phenomena have been presented [1–14], we focus on the semiconductor-based universal magnetologic gate (MLG) proposed by Dery *et al.* [11], where the operand of logic operation is the magnetization direction. The MLG consists of five elongated ferromagnetic electrodes with parallel easy-magnetization axes lined up on one semiconductor channel [Fig. 1(a)]. The two collinear easy axes, $+y$ and $-y$, are defined as the binary states 1 and 0, respectively. The two outmost ferromagnetic electrodes (FM-A and FM-A′) are input terminals, the center electrode (FM-M) is the output terminal, and the other electrodes (FM-B and FM-B′)

are configuration terminals that define the gate operation (e.g., NAND or OR). The MLG operates as a NAND (OR) gate when the magnetizations of FM-B and FM-B′ are both 1 (0). By application of charge currents between FM-A (FM-A′) and FM-B (FM-B′), spin accumulation is generated in the semiconductor channel, whose amplitude beneath the FM-M contact is represented by OR[exclusive-OR (XOR)(A, B), XOR(A′, B′)]. The output signal detected by FM-M is a spin-dependent voltage or a spin-dependent charge current. Any binary logic operation can be realized by using a finite number of MLGs. Furthermore, the ability to reconfigure logic gates at a clock frequency provides flexibility in logic circuit design, which enables a decrease in the number of gates and the time delay. A Boolean expression corresponds to a MLG consisting of two XOR gates. Therefore, logic operation of one XOR gate using three ferromagnetic electrodes (i.e., FM-A, FM-B, and FM-M) is a fundamental technique to realize MLG operation. XOR-gate operation has been demonstrated in graphene-based lateral spin devices at room temperature [15]. However, no implementation of XOR operation in a nondegenerate semiconductor, such as silicon (Si), has been demonstrated. Graphene is an atomically thin material, and its physical properties, such as conductivity and

*ando@kuee.kyoto-u.ac.jp
†mshiraishi@kuee.kyoto-u.ac.jp

carrier types, are strongly affected by adsorbents; that is, graphene does not tolerate contamination [16–18]. Meanwhile, Si is quite stable and robust to the surrounding environment in terms of its physical properties. Furthermore, a gate function using a metal-oxide-semiconductor structure for modulation of the electron conductivity has been established in Si, which is indispensable for the operation of a MLG with low power consumption. In a practical MLG logic circuit, a clock for simultaneous operation of all MLGs can be constructed in two ways: magnetization rotation of FM-M or gate modulation of the channel conductivity. From the point of view of the energy consumption and magnetic stability of the other ferromagnetic electrodes, the latter method is desired. The energy consumption for constructing one clock in the latter way is estimated to be at least 10 times smaller than that for constructing one clock in the former way [19,20]. For Si-based devices, efficient modulation of the conductivity of more than 6 orders of magnitude has already been established in lateral spin devices, and significant modulations of the electron conductivity and spin-accumulation voltage have been demonstrated [21,22]. Modulation of the spin-transport length using an electric field, well known as the "spin-drift effect", has also been demonstrated in both degenerate and nondegenerate Si spin devices, which is a key technique for XOR operation [23–29]. Furthermore, long-range spin transport due to the low spin scattering probability in the Si channel [30–32] and highly spin-polarized spin injection using Fe/MgO epitaxial layers [33] have also been reported, which are general requirements for highly efficient logic operation using a spin current.

In this study, room-temperature operation of an XOR gate is demonstrated with Fe/Co/MgO/Si multiterminal lateral spin devices. By adjustment of the charge current in the nondegenerate Si channel, which can control the spin-drift effect, clear XOR signals are obtained for several devices. In addition, detection of a spin-dependent charge current, (i.e., a charge current controlled by the XOR gate) is also demonstrated, which is key for operation of multiple MLGs using a thyristor latch. Furthermore, back-gate modulation of the XOR-gate operation is also realized, which is useful for operation of multiple XOR gates.

II. DEVICE FABRICATION AND NONLOCAL FOUR-TERMINAL MEASUREMENTS

Silicon-on-insulator substrates, consisting of a 100-nm-thick Si(100) layer/200-nm-thick buried SiO_2 layer/625-μm-thick Si(100) substrate, were used for fabrication of nondegenerate Si-based multiterminal lateral spin valves for XOR operation. Phosphorus (P) was ion implanted into the Si layer at a concentration of approximately $(3 \pm 2) \times 10^{17}$ cm^{-3} with a small distribution along the z direction because of the ion-implantation

technique. The conductivity of the Si channel (σ_{Si}) measured with a conventional four-terminal method was 1.93×10^3 Ω^{-1} m^{-1} at 300 K, indicating almost all dopants are activated. Before deposition of ferromagnetic metal/tunnel-barrier layers, a 20-nm-thick highly doped silicon epitaxial layer is grown by magnetron sputtering to suppress the depletion-layer thickness. Au(3 nm)/Fe(12.4 nm)/Co(0.6 nm)/MgO(0.8 nm) layers are subsequently deposited on the Si channel by molecular-beam epitaxy. After deposition of the layers, a Si spin channel with three ferromagnetic contacts (FM-A, FM-B, and FM-M) is fabricated by electron-beam lithography and argon-ion (Ar$^+$) milling. The top surface of the Si spin channel is etched to remove 20 nm of the highly doped silicon layer. Finally, two outer nonmagnetic electrodes (NM1 and NM2) are fabricated. Figure 1(b) shows a schematic of the typical device structure. In the XOR operation, a charge current is applied between FM-A and FM-B, where FM-A (FM-B) is under spin-injection (extraction) conditions. The spin-accumulation voltage is measured between FM-M and NM2. We fabricate several devices (devices A, B, C, and D) with different device geometries. The electrode widths of FM-A (w_A), FM-B (w_B), and FM-M (w_M) are 2, 0.8, and 0.2 μm, respectively. The center-to-center distances between adjacent electrodes (d_{AB} and d_{BM}) are $d_{AB} = 3.0$ μm and $d_{BM} = 1.5$ μm for device A and device B, respectively, and $d_{AB} = 21$ μm and $d_{BM} = 1.5$ μm for device C and device D, respectively. All measurements are performed at 300 K by a direct-charge-current technique with a commercial dc source meter and a digital multimeter.

First, we implement nonlocal four-terminal magnetoresistance (NLMR) measurements to investigate the spin-transport parameters of the fabricated devices, in which a magnetic field is applied along the $\pm y$ direction to control the magnetization configuration. Figures 1(c)–1(e) show typical NLMR signals measured at 300 K. The spin injector and detector are FM-A and FM-B [Fig. 1(c)], FM-B and FM-M [Fig. 1(d)], and FM-A and FM-M [Fig. 1(e)], respectively. The magnetization directions of each electrode are also displayed in Figs 1(c)–1(e). Clear rectangular signals are detected for all spin-injector and spin-detector combinations, indicating that all electrodes have finite spin polarization. The magnetic flux density, B_y, for magnetization switching of FM-A, FM-B, and FM-M is approximately 7, 16, and 36 mT, respectively. A considerable spin signal is also detected with the FM-A spin injector and the FM-M spin detector, even though FM-B is located between the two electrodes, indicating that the spin absorption by FM-B is negligibly small owing to the existence of the MgO tunnel barrier [34–36]. The magnitude of the NLMR signals, ΔV_s, as a function of the center-to-center distance between the spin injector and the spin detector, d, is displayed in Fig. 1(f). ΔV_s monotonically decreases with increasing d. The spin-diffusion length λ_s
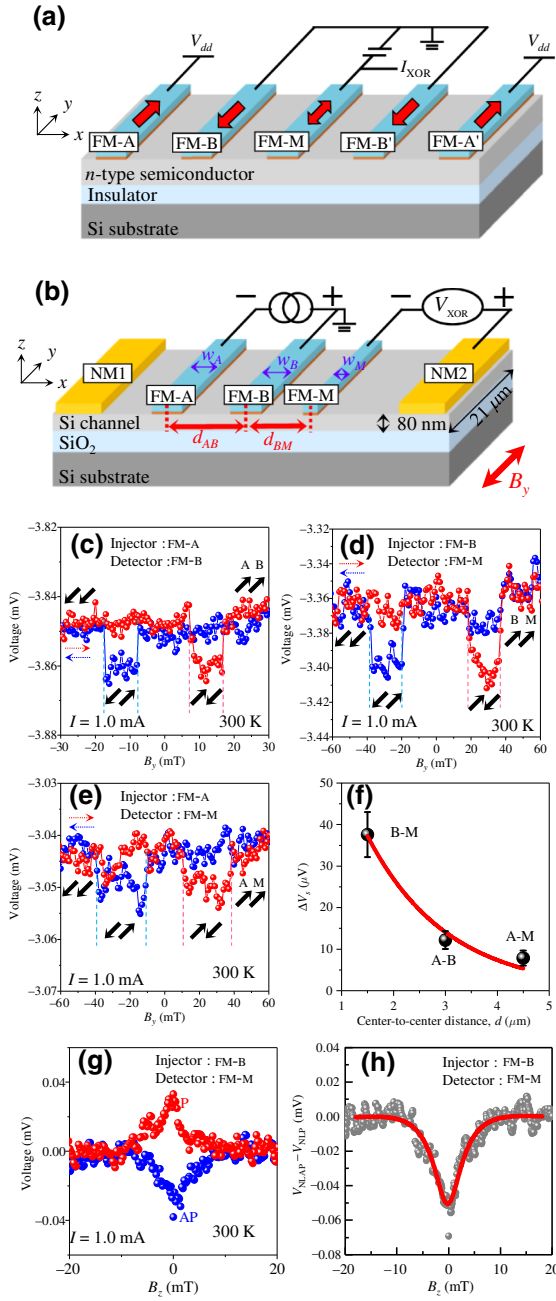
FIG. 1.   (a) The semiconductor-based MLG device proposed by Dery *et al.* [11]. (b) Silicon-based multiterminal lateral spin valves for XOR operation. (c)–(e) NLMR measured at 300 K. The spin injector and detector are (c) FM-A and FM-B, (d) FM-B and FM-M, and (e) FM-A and FM-M, respectively. (f) Dependence of the magnitude of NLMR signals on the center-to-center distance between the spin injector and the spin detector, d. The dots are experimental data, and the red line is a fitting result obtained with Eq. (1). (g) Hanle-effect signals under parallel (red) and antiparallel (blue) configurations, where the linear background is subtracted. The spin injector and the spin detector are FM-B and FM-M, respectively. (h) Difference in the Hanle signal between the antiparallel and parallel configurations. The dots and the solid line are the experimental data and the fitting curve obtained with Eq. (2).

is estimated to be 1.54 ± 0.30 μm by use of the following fitting function:

$$\Delta V_s = V_0 \exp\left(\frac{-d}{\lambda_s}\right). \quad (1)$$

Successful fitting also indicates negligible spin absorption by FM-B. Hanle-effect measurements are also performed between FM-B and FM-M, in which a magnetic field is applied along the $\pm z$ direction. Clear peak and dip features are observed under the parallel and antiparallel configurations, respectively, as shown in Fig. 1(g), indicating successful spin manipulation by the magnetic field. In the analysis, we calculate the difference in the nonlocal voltage between the antiparallel and parallel configurations as shown in Fig. 1(h) and use the following fitting function [37–40]:

$$\frac{V_{\text{NLAP}}(B_z) - V_{\text{NLP}}(B_z)}{I} = \frac{P^2 \lambda_s}{\sigma_{\text{Si}} A}(1 + \omega^2 \tau_s^2)^{-\frac{1}{4}} \exp$$

$$\left(-\frac{d}{\lambda_s}\sqrt{\frac{\sqrt{1 + \omega^2 \tau_s^2} + 1}{2}}\right)$$

$$\times \left[\cos\left(\frac{\arctan \omega\tau_s}{2} + \frac{d}{\lambda_s}\sqrt{\frac{\sqrt{1 + \omega^2 \tau_s^2} - 1}{2}}\right)\right], \quad (2)$$

where V_{NLAP} (V_{NLP}) is the nonlocal voltage under the antiparallel (parallel) configuration, τ_s is the spin lifetime in the Si channel, B_z is the magnetic flux density along the z direction, P is the spin polarization, A is the cross-sectional area of the channel, $\omega = g\mu_B B/\hbar$ is the Larmor frequency, g is the g factor for the electrons ($g = 2$ in this study), μ_B is the Bohr magneton, and $\hbar$ is the Dirac constant. From the analysis, λ_s and τ_s are estimated to be 1.41 ± 0.16 μm and 2.04 ± 0.16 ns, respectively, which is consistent with the results in Fig. 1(f) and those of a previous study [31].

III. XOR OPERATION

In the XOR operation, a direct charge current is applied from FM-A to FM-B, and the spin-accumulation voltage is measured by FM-M with reference to NM2. The magnetization direction of FM-M is fixed along the $+y$ direction. In this situation, the spin-accumulation voltage, V_{XOR}, detected by FM-M is expressed as $V_{\text{XOR}} = (\sigma_\uparrow \mu_\uparrow + \sigma_\downarrow \mu_\downarrow)/[e(\sigma_\uparrow + \sigma_\downarrow)]$, where $\sigma_\uparrow$ ($\sigma_\downarrow$) is the conductivity of up (down) spins in FM-M, e is the elementary charge and $\mu_\uparrow$ ($\mu_\downarrow$) is the electrochemical potential of up (down) spins at the Si/FM-M interface. When the electrochemical potential in Si beneath FM-M—that is, ($\mu_\uparrow + \mu_\downarrow$)—is set to be 0 meV, $\mu_\uparrow$ and $\mu_\downarrow$ have the same amplitude but opposite sign; namely, $\mu_\uparrow = -\mu_\downarrow$. In this case,

V_{XOR} is expressed as $V_{XOR} = (\sigma_\uparrow - \sigma_\downarrow)\mu_\uparrow/[e(\sigma_\uparrow + \sigma_\downarrow)]$ $= P_M\mu_\uparrow/e$, where P_M is the spin polarization of FM-M. Therefore, here we focus on $\mu_\uparrow$. $\mu_\uparrow$ in the nondegenerate Si channel under each magnetic configuration calculated by the one-dimensional spin-drift–spin-diffusion model is shown in Figs. 2(a) and 2(b). The magnetic configuration is denoted as $[A_\uparrow, B_\uparrow]$, $[A_\downarrow, B_\downarrow]$, $[A_\uparrow, B_\downarrow]$, and $[A_\downarrow, B_\uparrow]$, where A (B) and the suffix correspond to FM-A (FM-B) and its magnetization direction, respectively. The potential drop due to the electric field is eliminated for convenience of discussion [29]. In the calculation, d_{AB} and d_{BM} are fixed at 3.0 and 1.5 μm (i.e., FM-A, FM-B, and FM-M are located at $x = 0$, 3.0, and 4.5 μm, respectively). λ_s, σ_{Si} and P of the ferromagnetic electrodes are 1.5 μm, 3000 Ω^{-1} m^{-1}, and 8%, respectively, typical values in our Si spin valves. Under the parallel configuration, the directions of the spins injected from FM-A and those left in the Si channel after extraction from FM-B are opposite each other. The accumulated up (down) spins beneath FM-A (FM-B) are transported through the Si channel as a spin-diffusion current and a spin-drift current. As a result, the absolute value of V_{XOR} becomes smaller than that under the antiparallel configuration, in which the same orientation spins are accumulated beneath FM-A and FM-B. Here we focus on x_{con}, at which $\mu_\uparrow$ becomes 0 due to the equal numbers of up and down spins transported from FM-A and FM-B, respectively. At $I = 50$ μA, x_{con} is approximately 2.1 μm. Therefore, $\mu_\uparrow$ at FM-M ($x = 4.5$ μm) under each magnetic configuration ($[A_\uparrow, B_\uparrow]$, $[A_\downarrow, B_\downarrow]$, $[A_\uparrow, B_\downarrow]$, and $[A_\downarrow, B_\uparrow]$) represents four different values. In contrast, at $I = 200$ μA, x_{con} reaches $x = 3.0$ μm because of the enhanced spin-drift effect, resulting in the same $\mu_\uparrow$ for $[A_\uparrow, B_\uparrow]$ and $[A_\downarrow, B_\downarrow]$ at $x = 4.5$ μm. In this case, V_{XOR} represents three voltage levels. Figure 2(c) shows the current dependence of $\mu_\uparrow$ at $x = 4.5$ μm. $\mu_\uparrow$ at $[A_\uparrow, B_\downarrow]$ ($[A_\downarrow, B_\uparrow]$) monotonically increases (decreases) with increasing charge current. In contrast, that for $[A_\uparrow, B_\uparrow]$ and $[A_\downarrow, B_\downarrow]$ first decreases (increases), then (increases) decreases to 0 meV at a specific current I_0, and finally changes its polarity. Figures 2(d)–2(f) show the expected spin signals at $I < I_0$, $I = I_0$, and $I > I_0$, respectively, under the application of a magnetic field along the y direction. Here we suppose that the magnetization switching field of FM-M is designed to be higher than that of FM-A and FM-B and fixed along the $+y$ direction during the measurements. In the following, we label the spin-accumulation voltage under each magnetic configuration by $V_{\uparrow\uparrow}$, $V_{\downarrow\downarrow}$, $V_{\downarrow\uparrow}$, and $V_{\uparrow\downarrow}$, where the left (right) suffix is the magnetization direction of FM-A (FM-B). Since the polarity of $V_{\uparrow\uparrow} - V_{\downarrow\downarrow}$ depends on I, the shape of the hysteresis is drastically changed by changing I. These features of the hysteresis curves are expected in the spin XOR operation. The conventional NLMR as shown in Figs. 1(c)–1(e) can also be recognized as the XOR operation, because the spin-accumulation voltage is different between the parallel
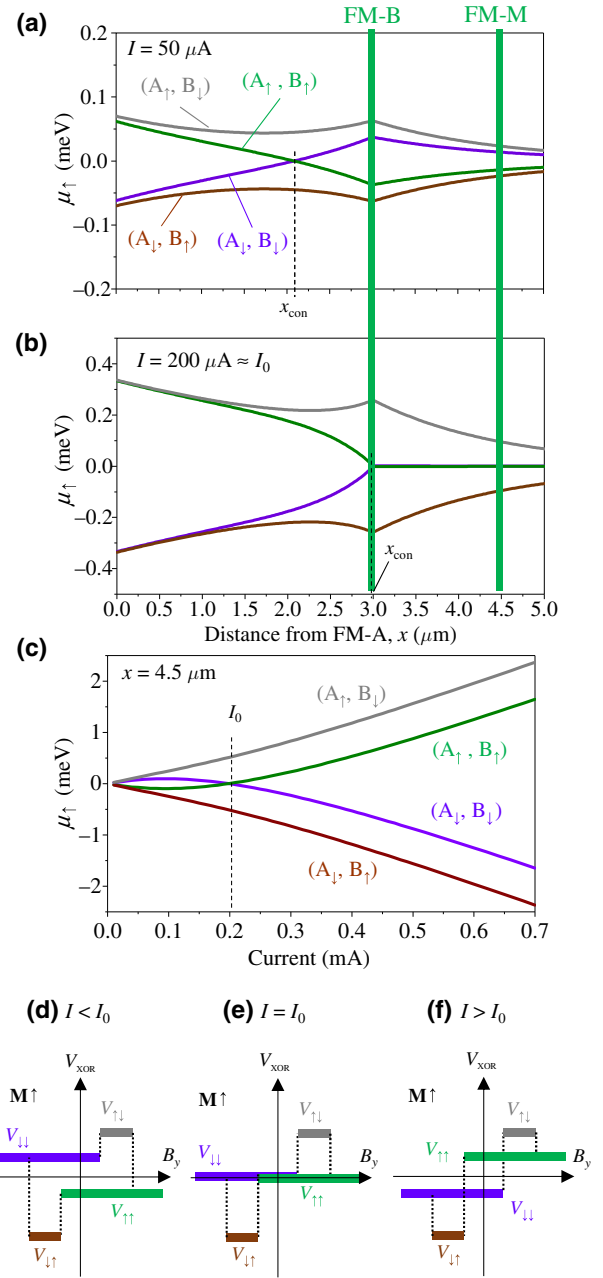

FIG. 2. The electrochemical potential of up spins, $\mu_\uparrow$, in the Si channel calculated by the one-dimensional spin-drift–spin-diffusion model. Because the potential drop due to the electric field is subtracted, the electrochemical potential of down spins, $\mu_\downarrow$, has the same value but opposite sign. Magnetic configurations of FM-A and FM-B are denoted as $[A_{\uparrow(\downarrow)}, B_{\uparrow(\downarrow)}]$, where the suffix means the magnetization direction of each electrode. The applied charge current from FM-B to FM-A is (a) 50 μA and (b) 200 μA. The center-to-center distances between FM-A and FM-B (d_{AB}) and between FM-B and FM-M (d_{BM}) are 3.0 and 1.5 μm, respectively. σ_{Si} and λ_s are 3000 Ω^{-1} m^{-1} and 1.5 μm, respectively. (c) Charge-current dependence of $\mu_\uparrow$ under various magnetic configurations of FM-A and FM-B; that is, $[A_\uparrow, B_\uparrow]$, $[A_\downarrow, B_\downarrow]$, $[A_\uparrow, B_\downarrow]$, and $[A_\downarrow, B_\uparrow]$. (d)–(f) Expected V_{XOR}-B_y signal shapes detected by FM-M at (d) $I < I_0$, (e) $I = I_0$, and (f) $I > I_0$.

(a) Device A

(b) Device B

(c) Device C

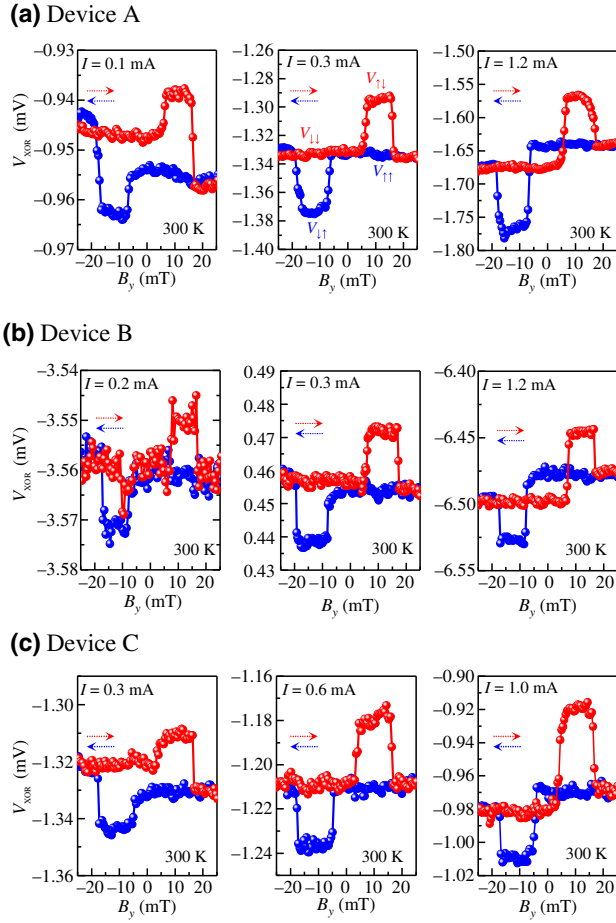FIG. 3. V_{XOR}-B_y curves at various charge currents for (a) device A, (b) device B, and (c) device C measured at room temperature. The distance between FM-A and FM-B is (a) 3.0 μm, (b) 3.0 μm, and (c) 21 μm. The magnetization of FM-M is fixed along the $+y$ direction. The external magnetic flux density, B_y, is swept between -30 and 30 mT, which is sufficiently small for magnetization switching of FM-M.

and antiparallel configurations. However, this feature is not applicable for the NAND or OR operation in the MLG. If we use the NLMR signals as a component of the MLG, the device consists of three center ferromagnetic electrodes (FM-B, FM-M, and FM-B′) and two outmost nonmagnetic electrodes (NM-A and NM-A′). In that case, the output voltage detected by FM-M exhibits the 0 state when the magnetization directions of FM-B and FM-B′ are (1, 0) or (0, 1) and the 1 state when they are (1, 1) or (0, 0). This gate is not a NAND gate or an OR gate but is an XOR gate. In other words, even though we increase the number of electrodes from three to five, the logic operation is still an XOR gate. Furthermore, a reconstruction of the logic gate is impossible by use of three ferromagnetic electrodes because two electrodes are used as the input terminals and the other electrode is used as the output terminal.

The magnetic field dependence of the spin-accumulation voltage, V_{XOR}, measured between FM-M and NM2 at 300 K is shown in Figs. 3(a)–3(c). A charge current is applied from FM-B to FM-A. The magnetization of FM-M is fixed along the $+y$ direction. The applied B_y is in the range from -30 to 30 mT, which is sufficiently small for magnetization switching of FM-M (36 mT), as confirmed in Figs. 1(c)–1(e). For device A, $V_{\uparrow\uparrow}$ is less than $V_{\downarrow\downarrow}$ at $I = 0.1$ mA, corresponding to Fig. 2(d), indicating an insufficient spin-drift effect. At $I = 0.3$ mA $\approx I_0$, $V_{\uparrow\uparrow} = V_{\downarrow\downarrow}$ is realized, resulting in the V_{XOR}-B_y curve with a three-voltage-level system, a successful demonstration of the XOR operation. At a charge current higher than I_0, the V_{XOR}-B_y curve shows four different values with $V_{\downarrow\downarrow} < V_{\uparrow\uparrow}$, corresponding to Fig. 2(f). Although similar signals are obtained at $I = 0.3$ and 1.2 mA for device B, the signal-to-noise ratio becomes lower below 0.2 mA, and no signals are detected at 0.1 mA because of the small charge current. Despite having the same device geometry, devices A and B exhibit several differences. First, the signal amplitude (the difference between $V_{\downarrow\uparrow}$ and $V_{\uparrow\downarrow}$) of device A is larger than that of device B for all I conditions, and a clear signal is detected at $I = 0.1$ mA only for device A. Second, $V_{\downarrow\downarrow}$ is slightly larger than $V_{\uparrow\uparrow}$ for device B at $I = 0.3$ mA, indicating that the I_0 condition is slightly shifted. Such a difference might be due to the slight difference in the spin polarization of the ferromagnetic electrodes and/or σ_{Si} of the Si channel. When the spin polarization of FM-M is decreased, the signal amplitude also decreases for all I regions and finally drops to below the detection limit. In contrast, when the spin polarization of FM-A or FM-B or σ_{Si} is modulated, the I_0 condition is changed. When the spin polarization of FM-B is changed from 8% to 10% in the situation for Fig. 2, the I_0 condition is estimated to change from 0.20 to 0.23 mA. Therefore, precise control of the spin polarization of the ferromagnetic electrodes and σ_{Si} of the channel is strongly desired for reliable operation of multiple MLGs. To meet such demanding requirements, a way to adjust the I_0 condition even for devices with scattered spin polarizations and/or σ_{Si} is discussed in Sec. V.

We also demonstrate XOR operation with large d_{AB} [Fig. 3(c)]. A clear XOR-operated signal is obtained at $I = 0.6$ mA $\approx I_0$. Since d_{AB} is 21 μm for device C, a large I_0 (0.6 mA) is obtained due to a further spin-drift effect that shifts the x_{con} point to $x = 21$ μm. The long-distance XOR operation enables the addition of several ferromagnetic electrodes between FM-A and FM-B to realize a high degree of design freedom. Because of the negligible spin absorption by the ferromagnetic electrode, we can freely add additional spin injectors. Spin-logic gates other than the MLG, such as a majority circuit, can be realized using multiple ferromagnetic electrodes. The charge-current dependences of $V_{\uparrow\uparrow}$, $V_{\downarrow\downarrow}$, $V_{\downarrow\uparrow}$, and $V_{\uparrow\downarrow}$ are summarized in Fig. 4 for devices B and C,
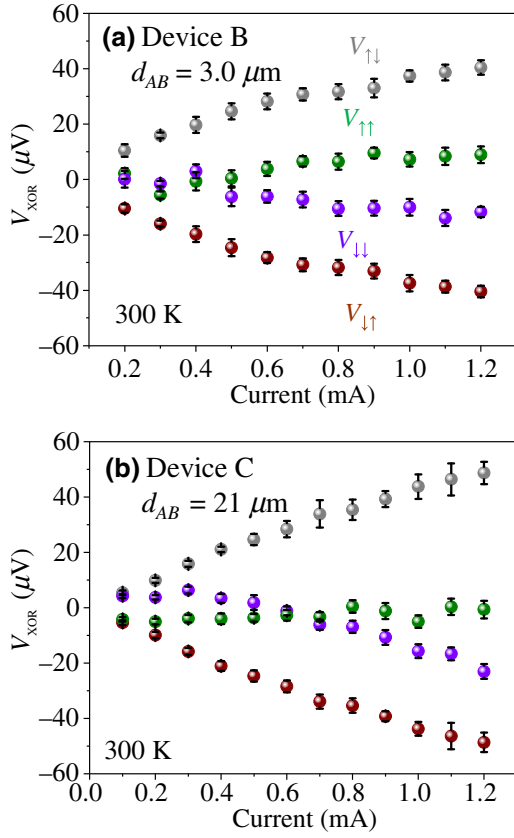
FIG. 4. Charge-current dependence of $V_{\uparrow\uparrow}$, $V_{\downarrow\downarrow}$, $V_{\downarrow\uparrow}$, and $V_{\uparrow\downarrow}$ for (a) device B and (b) device C, where the left (right) suffix is the magnetization direction of FM-A (FM-B). $(V_{\downarrow\uparrow} + V_{\uparrow\downarrow})/2$ is subtracted as a background voltage.

FIG. 5. (a) Current-voltage configuration for detection of the XOR-operated charge current. (b)–(d) XOR-operated charge current, I_{XOR}, as a function of B_y measured at 300 K for device B. The resistance of R_{XOR} is (b) 100 Ω, 1 kΩ, and 100 kΩ. The applied charge current is 0.3 mA. (f) ΔI_{XOR} as a function of R_{XOR}. The dots and the solid line are the experimental data and the fitting curve obtained with Eq. (3).

where $(V_{\downarrow\uparrow} + V_{\uparrow\downarrow})/2$ is subtracted as a background voltage. Although the behaviors qualitatively correspond to the theoretical ones shown in Fig. 2(c), there are several differences. For example, charge-current dependences of the absolute values of $V_{\downarrow\uparrow}$ and $V_{\uparrow\downarrow}$ show superlinear characteristics in the theoretical results, whereas the experimental ones show sublinear characteristics. Such a difference is caused by the reduction in the effective spin polarization of the injected current P_{inj}. In a previous study, we investigated charge-current, I_{inj}, dependence of P_{inj} in Si-based spin valves. It was revealed that P_{inj} was almost constant below $I_{inj} = 0.5$ mA [36]. In contrast, P_{inj} was decreased with increasing I_{inj} above 0.5 mA, mainly because the spin-resistance mismatch became pronounced due to the reduction in the interface resistance. In Fig. 4, the sublinear characteristics occur at approximately $I = 0.5$ mA.

IV. CHARGE-CURRENT DETECTION OF THE XOR GATE

In the MLG operation, a spin-dependent charge current is expected as an output signal to operate the next MLG via a thyristor. Therefore, detection of the XOR-operated
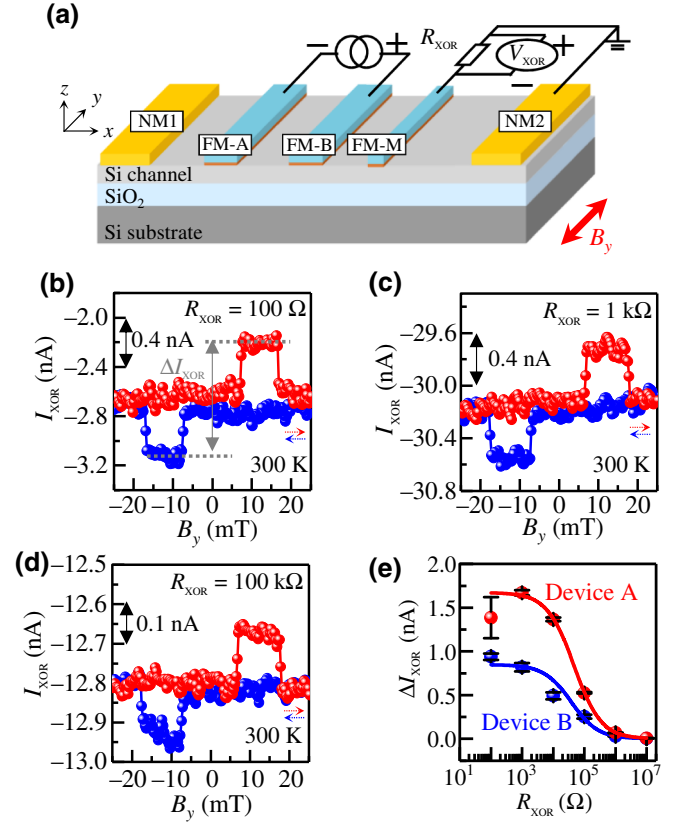
charge current, I_{XOR}, was also performed. The current-voltage configuration is shown in Fig. 5(a). Instead of the digital multimeter, a resistor, R_{XOR}, is inserted between FM-M and NM2. The resistance of R_{XOR} is much smaller than that of the internal resistor of the digital multimeter (more than 10 GΩ). Typical results for device B are shown in Figs. 5(b)–5(d), where I is 0.3 mA. The resistance of R_{XOR} is 100 Ω in Fig. 5(b), 1 kΩ in Fig. 5(c), and 100 kΩ in Fig. 5(d). I_{XOR} is calculated from the voltage drop at R_{XOR}. A clear XOR operation is also demonstrated even for the current-detection conditions. Except for the magnitude of the signals, no significant change is found over a wide range of R_{XOR}. The magnitudes of the output signals ΔI_{XOR} (i.e., the difference in I_{XOR} between two different antiparallel conditions) as a function of R_{XOR} for devices A and B are summarized in Fig. 5(e). The maximum ΔI_{XOR} is 1.67 nA, the highest value reported thus far. We use the following fitting function:

$$\Delta I_{XOR} = \frac{V_{\uparrow\downarrow} - V_{\downarrow\uparrow}}{R_{XOR} + R_{device}}, \tag{3}$$
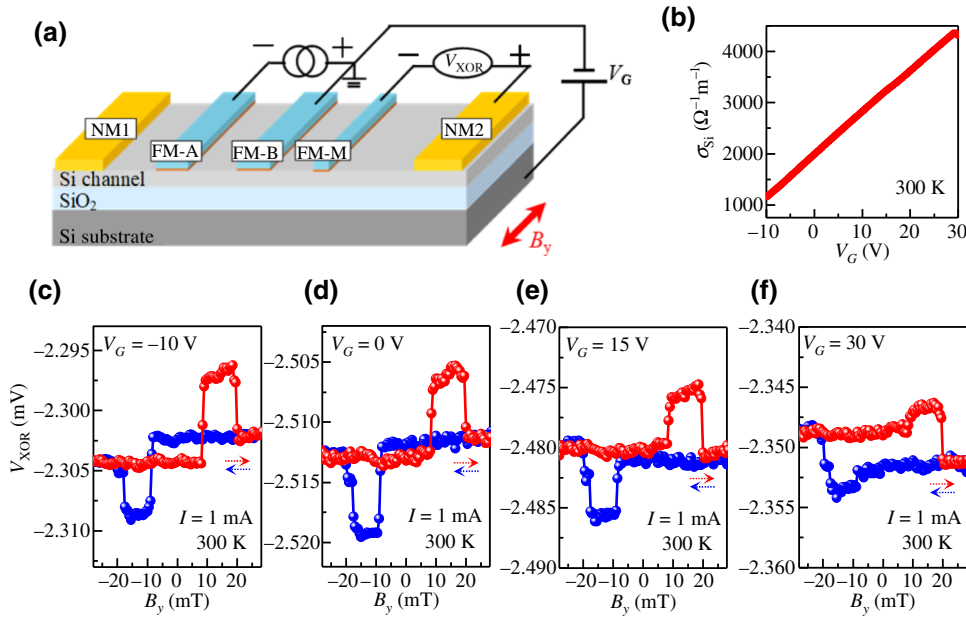
FIG. 6. (a) Current-voltage configuration for demonstration of gate modulation of the spin XOR operation. (b) Dependence of the conductivity of the Si channel, σ_{Si}, measured at 300 K on the back-gate voltage, V_G. (c)–(f) V_{XOR}-B_y curves at (c) $V_G = -10$ V, (d) $V_G = 0$ V, (e) $V_G = 15$ V, and (e) $V_G = 30$ V for device D. d_{AB} and d_{BM} of device D are 21 and 1.5 μm, respectively. The electric field through the SiO$_2$ layer is +150 MV m^{-1} at $V_G = +30$ V.

where R_{device} is the two-terminal resistance between FM-M and NM2. When we use experimentally obtained $V_{\downarrow\uparrow} - V_{\uparrow\downarrow}$ from Figs. 3(a) and 3(b), the fitting curve nicely reproduces the experimental data. R_{device} for device A and device B is estimated to be 46.8 ± 2 and 37.6 ± 3 kΩ, respectively, consistent with the resistance at zero bias in previous studies [29]. Because of the considerable parasitic resistance, the maximum ΔI_{XOR} is limited to be around 1.67 nA, which is larger than the shot-noise level in the operation at 0.1 GHz, but less than the Johnson thermal noise current [11]. However, a 10–100-fold larger ΔI_{XOR} is possible by reduction of the parasitic resistance, increase of P, and decreases of d_{AB} and d_{BM}. P of the Fe/MgO contact was approximately 5% for device A and approximately 3% for device B, values slightly smaller than in our previous studies. A tenfold increase of P might be possible by use of highly-spin-polarized materials such as Heusler alloys. The spin split of the electrochemical potential due to the spin accumulation in the Si channel underneath FM-B is approximately 2 meV at an injected current density of 1.79 kA cm^{-2} for device A. It decreases by around 60%–70% underneath FM-M because d_{BM} is comparable to λ_s.

V. OPERATION OF A GATE-TUNABLE XOR LOGIC GATE

In Sec. III, we reported scattered I_0 probably due to the scattered spin polarization and/or σ_{Si} despite the same device geometries. In this section, we demonstrate gate modulation of the XOR operation to control the I_0 condition. A back gate, V_G, is applied to control σ_{Si} and the spin-drift effect as shown in Fig. 6(a). The V_G dependence

of σ_{Si} is displayed in Fig. 6(b). σ_{Si} is modulated by more than 4 times by our changing V_G from -10 to $+30$ V. V_G-dependent V_{XOR}-B_y curves at $I = 1.0$ mA for device D are shown in Figs. 6(c)–6(f). At $V_G = 0$ V [Fig. 6(d)], whereas a clear signal is detected, $V_{\downarrow\downarrow}$ is slightly smaller than $V_{\uparrow\uparrow}$, indicating $I_0 < 1.0$ mA. In contrast, at $V_G = +15$ V [Fig. 6(e)], $V_{\downarrow\downarrow}$ becomes larger than $V_{\uparrow\uparrow}$, indicating $I_0 > 1.0$ mA. The difference between $V_{\downarrow\downarrow}$ and $V_{\uparrow\uparrow}$ becomes pronounced at $V_G = 30$ V [Fig. 6(c), $I_0 < 1.0$ mA] and -10 V [Fig. 6(f), $I_0 > 1.0$ mA]. Therefore, the systematic modulation of the I_0 condition is successfully realized by application of V_G.

Hereafter, we discuss the advantages of the gate modulation of the XOR gate. In practical spin-current logic gates such as MLGs, many devices should be combined. For reliable operation, I_0 should be designed with the same value. However, I_0 is scattered because of the immaturity of device-fabrication technology, as discussed in Sec. III. Even for the mature Si CMOS technology, this problem becomes pronounced because of the dispersion of the number of dopant atoms, which impedes further progress in Moore's law. In contrast, in our spin-current device, the threshold condition can be controlled after fabrication by use of a gate function, which is a great advantage over the conventional CMOS device. If a floating gate is fabricated on the Si channel, then such an adjustment is easily realized with nonvolatility. Such a threshold modulation can be useful, similar to the body effect in a conventional metal-oxide-semiconductor field-effect transistor. In Fig. 6, gate modulation of the XOR operation is demonstrated under constant-current application, because we focus on the MLG application. Under the constant-voltage condition, both the I_0 condition and the

magnitude of the spin signal are expected to change. Such a modulation is also useful for weighting algorithms controlled by floating gates.

VI. CONCLUSION

In conclusion, we demonstrate room-temperature XOR operation in Fe/Co/MgO/Si lateral spin devices. By adjustment of the in-plane electric field in the Si channel, clear XOR-operated hysteresis signals are detected for several devices with different channel lengths. XOR operation over a long channel distance of 21 μm enables a high degree of design freedom for multiterminal ferromagnetic electrodes. Charge-current detection of the XOR operation is also demonstrated. Furthermore, the charge-current condition for the XOR operation is modulated by a gate function, which is a great advantage for multiple-MLG operation. Whereas an external magnetic field is used to control the magnetic configuration in this study, individual control of each magnetization in multiple ferromagnetic electrodes becomes difficult, such as in an MLG. For the practical use of MLGs, use of spin-orbit torque or voltage-induced magnetization switching is desired [41–44]. Demonstration of a spin-logic gate by use of the magnetic proximity effect instead of conventional electrical spin injection through ferromagnetic metals is also worthy of study. Several studies have reported that the sign and the magnitude of the spin polarization in the magnetically proximitized layer can be controlled by the gate function [45–48]. Such a sign reversal of the spin polarization can be useful for ultrafast switching of the logic configuration in an MLG at a clock frequency.

ACKNOWLEDGMENT

———————

[1] D. A. Allwood, Gang Xiong, M. D. Cooke, C. C. Faulkner, D. Atkinson, N. Vernier, and R. P. Cowburn, Submicrometer ferromagnetic NOT gate and shift register, Science **296,** 2003 (2002).

[2] M. E. Flatté, Z. G. Yu, E. Johnston-Halperin, and D. D. Awschalom, Theory of semiconductor magnetic bipolar transistors, Appl. Phys. Lett. **82,** 4740 (2003).

[3] M. Zeng, L. Shen, H. Su, C. Zhang, and Y. Feng, Graphene-based spin logic gates, Appl. Phys. Lett. **98,** 092110 (2011).

[4] H. Dery, H. Wu, B. Ciftcioglu, M. Huang, Y. Song, R. Kawakami, J. Shi, I. Krivorotov, I. Žutić, and L. J. Sham, Nanospintronics based on magnetologic gates, IEEE Trans. Electron Devices **59,** 259 (2012).

[5] S. Manipatruni, D. E. Nikonov, and I. A. Young, Beyond CMOS computing with spin and polarization, Nat. Phys. **14,** 338 (2018).

[6] S. Manipatruni, D. E. Nikonov, C.-C. Lin, T. A. Gosavi, H. Liu, B. Prasad, Y.-L. Huang, E. Bonturim, R. Ramesh, and I. A. Young, Scalable energy-efficient magnetoelectric spin–orbit logic, Nature **565,** 35 (2019).

[7] J. Schliemann, J. C. Egues, and D. Loss, Nonballistic Spin-Field-Effect Transistor, Phys. Rev. Lett. **90,** 146801 (2003).

[8] S. Sugahara and M. Tanaka, A spin metal–oxide–semiconductor field-effect transistor using half-metallic-ferromagnet contacts for the source and drain, Appl. Phys. Lett. **84,** 2307 (2004).

[9] J. Fabian, I. Žutić, and S. Das Sarma, Magnetic bipolar transistor, Appl. Phys. Lett. **84,** 85 (2004).

[10] I. Žutić, J. Fabian, and S. Das Sarma, Spintronics: Fundamentals and applications, Rev. Mod. Phys. **76,** 323 (2004).

[11] H. Dery, P. Dalal, Ł Cywiński, and L. J. Sham, Spin-based logic in semiconductors for reconfigurable large-scale circuits, Nature **447,** 573 (2007).

[12] T. Schneider, A. A. Serga, B. Leven, B. Hillebrands, R. L. Stamps, and M. P. Kostylev, Realization of spin-wave logic gates, Appl. Phys. Lett. **92,** 022505 (2008).

[13] H. C. Koo, J. H. Kwon, J. Eom, J. Chang, S. H. Han, and M. Johnson, Control of spin precession in a spin-injected field effect transistor, Science **325,** 1515 (2009).

[14] B. Behin-Aein, D. Datta, S. Salahuddin, and S. Datta, Proposal for an all-spin logic device with built-in memory, Nat. Nanotechnol. **5,** 266 (2010).

[15] H. Wen, H. Dery, W. Amamou, T. Zhu, Z. Lin, J. Shi, I. Žutić, I. Krivorotov, L. J. Sham, and R. K. Kawakami, Experimental Demonstration of XOR Operation in Graphene Magnetologic Gates at Room Temperature, Phys. Rev. Appl. **5,** 044003 (2016).

[16] F. Schedin, A. K. Geim, S. V. Morozov, E. W. Hill, P. Blake, M. I. Katsnelson, and K. S. Novoselov, Detection of individual gas molecules adsorbed on graphene, Nat. Mater. **6,** 652 (2007).

[17] K. T. Chan, J. B. Neaton, and M. L. Cohen, First-principles study of metal adatom adsorption on graphene, Phys. Rev. B **77,** 235430 (2008).

[18] Y. Dan, Y. Lu, N. J. Kybert, Z. Luo, and A. T. C. Johnson, Intrinsic response of graphene vapor sensors, Nano Lett. **9,** 1472 (2009).

[19] H. Yoda *et al.*, High efficient spin transfer torque writing on perpendicular magnetic tunnel junctions for high density MRAMs, Curr. Appl. Phys. **10,** e87 (2010).

[20] S. Shirotori, H. Yoda, Y. Ohsawa, N. Shimomura, T. Inokuchi, Y. Kato, Y. Kamiguchi, K. Koi, K. Ikegami, H. Sugiyama, M. Shimizu, B. Altansargai, S. Oikawa, M. Ishikawa, A. Tiwari, Y. Saito, and A. Kurobe, Voltage-control spintronics memory with a self-aligned heavy-metal electrode, IEEE Trans. Magn. **53,** 3401104 (2017).

[21] Y. Ando, Y. Maeda, K. Kasahara, S. Yamada, K. Masaki, Y. Hoshi, K. Sawano, K. Izunome, A. Sakai, M. Miyao, and K. Hamaya, Electric-field control of spin accumulation signals in silicon at room temperature, Appl. Phys. Lett. **99,** 132511 (2011).

[22] T. Tahara, H. Koike, M. Kameno, T. Sasaki, Y. Ando, K. Tanaka, S. Miwa, Y. Suzuki, and M. Shiraishi, Room-temperature operation of Si spin MOSFET with high on/off spin signal ratio, Appl. Phys. Express **8,** 113004 (2015).

[23] A. G. Aronov and G. E. Pikus, Spin injection into semiconductors, Sov. Phys. Semicond **10**, 698 (1976). [Fiz. Tekh. Poluprovodn. 10, 1177 (1976)].

[24] I. Žutić, J. Fabian, and S. Das Sarma, Spin injection through the depletion layer: A theory of spin-polarized p-n junctions and solar cells, Phys. Rev. B **64**, 121201 (2001).

[25] Z. G. Yu and M. E. Flatté, Spin diffusion and injection in semiconductor structures: Electric field effects, Phys. Rev. B **66**, 235302 (2002).

[26] Z. G. Yu and M. E. Flatté, Electric-field dependent spin diffusion and spin injection into semiconductors, Phys. Rev. B **66**, 201202 (2002).

[27] J. Fabian, I. Žutić, and S. Das Sarma, Theory of spin-polarized bipolar transport in magnetic p-n junctions, Phys. Rev. B **66**, 165301 (2002).

[28] M. Kameno, Y. Ando, T. Shinjo, H. Koike, T. Sasaki, T. Oikawa, T. Suzuki, and M. Shiraishi, Spin drift in highly doped n-type Si, Appl. Phys. Lett. **104**, 092409 (2014).

[29] T. Tahara, Y. Ando, M. Kameno, H. Koike, K. Tanaka, S. Miwa, Y. Suzuki, T. Sasaki, T. Oikawa, and M. Shiraishi, Observation of large spin accumulation voltages in nondegenerate Si spin devices due to spin drift effect: Experiments and theory, Phys. Rev. B **93**, 214406 (2016).

[30] B. Huang, D. J. Monsma, and I. Appelbaum, Coherent Spin Transport Through a 350 Micron Thick Silicon Wafer, Phys. Rev. Lett. **99**, 177209 (2007).

[31] T. Sasaki, Y. Ando, M. Kameno, T. Tahara, H. Koike, T. Oikawa, T. Suzuki, and M. Shiraishi, Spin Transport in Nondegenerate Si with a Spin MOSFET Structure at Room Temperature, Phys. Rev. Appl. **2**, 034005 (2014).

[32] S. Lee, N. Yamashita, Y. Ando, S. Miwa, Y. Suzuki, H. Koike, and M. Shiraishi, Investigation of spin scattering mechanism in silicon channels of Fe/MgO/Si lateral spin valves, Appl. Phys. Lett. **110**, 192401 (2017).

[33] A. Spiesser, H. Saito, Y. Fujita, S. Yamada, K. Hamaya, S. Yuasa, and R. Jansen, Giant Spin Accumulation in Silicon Nonlocal Spin-Transport Devices, Phys. Rev. Appl. **8**, 064023 (2017).

[34] G. Schmidt, D. Ferrand, L. W. Molenkamp, A. T. Filip, and B. J. van Wees, Fundamental obstacle for electrical spin injection from a ferromagnetic metal into a diffusive semiconductor, Phys. Rev. B **62**, R4790 (2000).

[35] A. Fert and H. Jaffrès, Conditions for efficient spin injection from a ferromagnetic metal into a semiconductor, Phys. Rev. B **64**, 184420 (2001).

[36] S. Lee, F. Rortais, R. Ohshima, Y. Ando, S. Miwa, Y. Suzuki, H. Koike, and M. Shiraishi, Quantitative and systematic analysis of bias dependence of spin accumulation voltage in a nondegenerate Si-based spin valve, Phys. Rev. B **99**, 064408 (2019).

[37] F. J. Jedema, H. R. Heersche, A. T. Filip, J. J. A. Baselmans, and B. J. van Wees, Electrical detection of spin precession in a metallic mesoscopic spin valve, Nature **416**, 713 (2002).

[38] T. Sasaki, T. Oikawa, T. Suzuki, M. Shiraishi, Y. Suzu, and K. Noguchi, Evidence of electrical spin injection into silicon using MgO tunnel barrier, IEEE Trans. Magn. **46**, 1436 (2010).

[39] T. Sasaki, T. Oikawa, M. Shiraishi, Y. Suzuki, and K. Noguchi, Comparison of spin signals in silicon between nonlocal four-terminal and three-terminal methods, Appl. Phys. Lett. **98**, 012508 (2011).

[40] T. Suzuki, T. Sasaki, T. Oikawa, M. Shiraishi, Y. Suzuki, and K. Noguchi, Room-Temperature electron spin transport in a highly doped Si channel, Appl. Phys. Express **4**, 023003 (2011).

[41] L. Liu, C.-F. Pai, Y. Li, H. W. Tseng, D. C. Ralph, and R. A. Buhrman, Spin-torque switching with the giant spin Hall effect of tantalum, Science **336**, 555 (2012).

[42] L. Liu, O. J. Lee, T. J. Gudmundsen, D. C. Ralph, and R. A. Buhrman, Current-Induced Switching of Perpendicularly Magnetized Magnetic Layers Using Spin Torque from the Spin Hall Effect, Phys. Rev. Lett. **109**, 096602 (2012).

[43] T. Maruyama, Y. Shiota, T. Nozaki, K. Ohta, N. Toda, M. Mizuguchi, A. A. Tulapurkar, T. Shinjo, M. Shiraishi, S. Mizukami, Y. Ando, and Y. Suzuki, Large voltage-induced magnetic anisotropy change in a few atomic layers of iron, Nat. Nanotechnol. **4**, 158 (2009).

[44] Y. Shiota, T. Nozaki, F. Bonell, S. Murakami, T. Shinjo, and Y. Suzuki, Induction of coherent magnetization switching in a few atomic layers of FeCo using voltage pulses, Nat. Mater. **11**, 39 (2012).

[45] S. Y. Huang, X. Fan, D. Qu, Y. P. Chen, W. G. Wang, J. Wu, T. Y. Chen, J. Q. Xiao, and C. L. Chien, Transport Magnetic Proximity Effects in Platinum, Phys. Rev. Lett. **109**, 107204 (2012).

[46] P. Lazić, K. D. Belashchenko, and I. Žutić, Effective gating and tunable magnetic proximity effects in two-dimensional heterostructures, Phys. Rev. B **93**, 241401 (2016).

[47] J. Xu, S. Singh, J. Katoch, G. Wu, T. Zhu, I. Žutić, and R. K. Kawakami, Spin inversion in graphene spin valves by gate-tunable magnetic proximity effect at one-dimensional contacts, Nat. Commun. **9**, 2869 (2018).

[48] I. Žutić, A. Matos-Abiague, B. Scharf, H. Dery, and K. Belashchenko, Proximitized materials, Mater. Today **22**, 85 (2019).